

# Direct numerical simulation of turbulent Taylor–Couette flow

S. DONG

Center for Computational and Applied Mathematics, Department of Mathematics,  
Purdue University, West Lafayette, IN 47907, USA

(Received 31 January 2007 and in revised form 14 May 2007)

We investigate the dynamical and statistical features of turbulent Taylor–Couette flow (for a radius ratio 0.5) through three-dimensional direct numerical simulations (DNS) at Reynolds numbers ranging from 1000 to 8000. We show that in three-dimensional space the Görtler vortices are randomly distributed in banded regions on the wall, concentrating at the outflow boundaries of Taylor vortex cells, which spread over the entire cylinder surface with increasing Reynolds number. Görtler vortices cause streaky structures that form herringbone-like patterns near the wall. For the Reynolds numbers studied here, the average axial spacing of the streaks is approximately 100 viscous wall units, and the average tilting angle ranges from  $16^\circ$  to  $20^\circ$ . Simulation results have been compared to the experimental data in the literature, and the flow dynamics and statistics are discussed in detail.

---

## 1. Introduction

Taylor–Couette flow becomes particularly complex as the Reynolds number increases. With increasing Reynolds number, the flow undergoes a series of transitions from circular Couette flow, to axially periodic Taylor vortex flow (Taylor 1923), to a state with waves on the vortices (Coles 1965; Coughlin *et al.* 1991), to chaotic and turbulent Taylor vortex flow (Coles 1965; Fernstermatcher, Swinney & Gollub 1979; Lathrop, Fineberg & Swinney 1992*a*; von Stamm *et al.* 1996; Parker & Merati 1996; Takeda 1999). In the cases considered in the present paper, the outer cylinder is fixed while the inner cylinder rotates at a constant angular velocity. We focus on values of the Reynolds number at which the flow becomes turbulent and small-scale azimuthal vortices dominate the regions close to both cylinder walls. As there is an overwhelming volume of literature on Taylor–Couette flows (see the review by DiPrima & Swinney 1981 and the references therein), in order to provide a perspective on the flow structures and statistics of Taylor–Couette turbulence herein, only related experimental and numerical investigations are reviewed in the sections that follow.

### *Parameter definitions*

It is necessary to first define several parameters before proceeding. The geometry of the flow is characterized by the radius ratio,  $\eta = R_1/R_2$ , where  $R_1$  and  $R_2$  are the radii of the inner and outer cylinders respectively, and the aspect ratio,  $\Gamma = L_z/d$ , where  $L_z$  is the axial dimension of the domain and  $d$  is the gap width,  $d = R_2 - R_1$ . We define the Reynolds number

$$Re = \frac{U_0 d}{\nu}, \quad (1.1)$$

where  $U_0$  is the rotation velocity of the inner cylinder and  $\nu$  the kinematic viscosity of the fluid. There are several definitions of the Taylor number  $Ta$  in the literature. Following Wei *et al.* (1992), we define it

$$Ta = (U_0^2 d^2 / \nu^2) (d / R_1) = Re^2 \left( \frac{1}{\eta} - 1 \right). \quad (1.2)$$

### *Experimental investigations*

Experimental measurement and flow visualization have been the predominant, if not the exclusive, source of our knowledge about Taylor–Couette flows in the turbulent regime. Insights into the scalings of the torque, velocity structural functions, mass transfer coefficient, and the effects of Reynolds number in Taylor–Couette turbulence are provided by the experiments in Wendt (1933), Donnelly & Simon (1959), Bilgen & Boulos (1973), Tam & Swinney (1987), Brandstater & Swinney (1987), Tong *et al.* (1990), Lathrop, Fineberg & Swinney (1992*a, b*), Lewis & Swinney (1999), She *et al.* (2001), van den Berg *et al.* (2003), and Racina & Kind (2006). A detailed analysis of the experimental data from several studies is available in Dubrulle *et al.* (2005).

Koschmieder (1979) measured the wavelengths of turbulent Taylor vortices (i.e. the distance between adjacent Taylor vortex pairs) at two radius ratios 0.727 and 0.896, and observed that the wavelength was substantially larger than that of laminar Taylor vortices at the critical onset Taylor number  $T_c$  (defined as the Taylor number at which the circular Couette flow transitions to the Taylor vortex flow). He also observed the existence of a continuum of steady non-unique states of the flow, a phenomenon first detailed by Coles (1965). The hot-wire anemometry measurements by Smith & Townsend (1982) and Townsend (1984) for a radius ratio 0.667 suggested that for Taylor numbers below  $3 \times 10^5 T_c$  turbulent Taylor vortices encircling the inner cylinder dominated the flow and were superimposed on a background of irregular motions. Beyond  $5 \times 10^5 T_c$  these turbulent vortices became fragmented and lost regularity, and the flow became completely turbulent.

Barcilon *et al.* (1979) studied the coherent structures in Taylor–Couette turbulence with visualizations for a radius ratio 0.908, and observed a fine herringbone-like pattern of streaks at the outer cylinder wall for Taylor numbers over  $400 T_c$ . They conjectured that these streaks were the inflow and outflow boundaries of Görtler vortices (Görtler 1954) in the boundary layer region. Assuming a wide separation of length scales of Taylor and Görtler instabilities at high Taylor numbers, Barcilon & Brindley (1984) proposed a mathematical model by partitioning the flow into interior (Taylor vortex) and boundary layer (Görtler vortex) regions and coupling these regions through matched asymptotic expansions. They computed the Görtler vortex scales based on this model and demonstrated good comparisons with experimental observations. To test the Görtler hypothesis of Barcilon *et al.* (1979) and Barcilon & Brindley (1984), Wei *et al.* (1992) performed laser-induced fluorescence flow visualizations for three radius ratios (0.084, 0.5 and 0.88) at moderately high Reynolds numbers. They observed that Görtler vortices appeared first near the inner cylinder wall, and at Taylor numbers an order of magnitude lower than those in Barcilon *et al.* (1979). In contrast, Barcilon *et al.* (1979) observed the herringbone streaks primarily at the outer cylinder wall, although Barcilon & Brindley (1984) commented on unpublished studies about observations of herringbone streaks at the inner cylinder wall as well.

*Numerical simulations*

Compared to experiments, numerical investigations of Taylor–Couette flow in the turbulent regime have lagged far behind. A survey of literature indicates that almost all the numerical simulations so far have concentrated on the laminar regime at low Reynolds numbers, including Taylor vortex flow (Mujumdar & Spalding 1977; Jones 1981, 1982; Fasel & Booz 1984; Cliffe & Mullin 1985; Jones 1985; Barenghi & Jones 1989; Rigopoulos, Sheridan & Thompson 2003), wavy vortex flow (Marcus 1984*a, b*; King *et al.* 1984; Moulic & Yao 1996; Riechelmann & Nanbu 1997; Czarny *et al.* 2004) and modulated wavy vortex flow (Coughlin *et al.* 1991; Coughlin & Marcus 1992*a, b*). Here we primarily restrict considerations to configurations with a fixed outer cylinder and no imposed axial flow.

Several studies have been conducted at higher Reynolds numbers on ‘turbulent bursts’ (Coughlin & Marcus 1996) and the chaotic behaviour of Taylor–Couette flow (Vastano & Moser 1991). In addition, steady-state quasi-two-dimensional (ignoring azimuthal dependence) Reynolds-averaged Navier–Stokes (RANS) simulations were performed by several researchers (Wild, Djilali & Vickers 1996; Batten, Bressloff & Turnock 2002) employing turbulence models.

In order to understand the mechanism of transition from quasi-periodicity to chaos observed in experiments (Brandstater & Swinney 1987), Vastano & Moser (1991) performed a short-time Lyapunov exponent analysis of the Taylor–Couette flow by simultaneously advancing the full numerical solution and a set of perturbations for a radius ratio 0.875 at Reynolds numbers between 1160 and 1340. A partial Lyapunov exponent spectrum was computed and the dimension of the chaotic attractor was estimated. Noting the concentration of perturbation fields on the outflow jet and other characteristics, they argued that the chaos-producing mechanism was a Kelvin–Helmholtz instability of the outflow boundary jet between counter-rotating Taylor vortices. More recently, Bilson & Bremhorst (2007) simulated the Taylor–Couette flow at Reynolds number 3200 for a radius ratio 0.617 using a second-order finite volume method. A comprehensive verification for several parameters was conducted, and the comparison with available experimental data showed an agreement of trends. A number of statistical quantities were studied, and results of Reynolds stress budgets indicated higher turbulence production and dissipation values near cylinder walls.

*Objective*

In this paper, we focus on the dynamics and statistics of small-scale near-wall azimuthal vortices in *turbulent* Taylor–Couette flow. For this purpose, we have performed three-dimensional direct numerical simulations at four Reynolds numbers, ranging from 1000 to 8000, for a radius ratio  $\eta = 0.5$ . While the flow remains laminar at the lowest Reynolds number  $Re = 1000$ , it becomes turbulent for the three higher Reynolds numbers. We demonstrate the herringbone-like patterns of streaks near cylinder walls that are reminiscent of the observations by Barcilon *et al.* (1979), and elucidate how the increase in Reynolds number affects the characteristics of these streaks and the Görtler vortices, as well as the distributions of statistical quantities.

**2. Simulation methodology and parameters**

Consider the incompressible flow between two infinitely long concentric cylinders. The cylinder axis is aligned with the  $z$ -axis of the coordinate system. The inner cylinder, with radius  $R_1$ , rotates counter-clockwise (viewed toward the  $-z$  direction) at a constant angular velocity  $\Omega$  while the outer cylinder, with radius  $R_2$ , is at rest. In

---

Cases	$N_z$	$P$	$L_z/d$	$C_{Tinner}$	$C_{Touter}$
A	128	6	$\pi$	-0.0125	0.0127
B	256	6	$2\pi$	-0.0126	0.0127
C	128	7	$\pi$	-0.0126	0.0126
D	256	7	$1.5\pi$	-0.0126	0.0126
E	256	7	$2\pi$	-0.0126	0.0127
F	128	8	$\pi$	-0.0128	0.0128
G	128	9	$\pi$	-0.0128	0.0128

---

TABLE 1. Grid resolution studies at  $Re=8000$ .  $N_z$ , number of Fourier planes in the axial direction;  $P$ , element order;  $C_{Tinner}$ , mean torque coefficient on inner cylinder wall;  $C_{Touter}$ , mean torque coefficient on outer cylinder wall.

the simulations, the coordinates and length variables are normalized by the cylinder gap width  $d$ ; The velocity components are normalized by the rotation velocity of the inner cylinder  $U_0 = \Omega R_1$ , and the pressure by  $\rho U_0^2$ , where  $\rho$  is the fluid density. So the Reynolds number is defined by Equation (1.1).

We solve the three-dimensional incompressible Navier-Stokes equations by employing a Fourier spectral expansion of flow variables in the  $z$ -direction (along the cylinder axis), assuming the flow is periodic at  $z=0$  and  $z=L_z$  (the axial dimension of the computational domain), and a spectral element discretization (Karniadakis & Sherwin 2005) of the annular domain in  $(x, y)$ -planes. For time integration we employ a stiffly stable velocity-correction-type scheme with a third-order accuracy in time (Karniadakis, Israeli & Orszag 1991). The above numerical scheme has been extensively used to study bluff-body flow and turbulence problems (Dong & Karniadakis 2005; Dong *et al.* 2006). No-slip boundary conditions are employed on the inner and outer cylinder walls.

We consider the Taylor–Couette flow at four Reynolds numbers,  $Re=1000, 3000, 5000$  and  $8000$ , for a radius ratio  $\eta=0.5$ . The axial dimension of the computational domain is varied between  $L_z/d=\pi$  and  $2\pi$ . Extensive grid refinement tests have been conducted. We employ a spectral element mesh with 400 quadrilateral elements in the  $(x, y)$ -planes, and the element order is varied from 6 to 9, with over-integration (Kirby & Karniadakis 2003). In the axial direction we employ 64 to 128 Fourier modes (or 128 to 256 grid points), with 3/2-dealiasing. These parameters lead to grid spacings near the cylinder surface, in viscous wall units, of 0.21 in the radial direction, 1.96 in the azimuthal direction and 3.70 in the axial direction for  $Re=8000$ , and 0.04 in the radial direction, 0.40 in the azimuthal direction and 0.76 in the axial direction for  $Re=1000$ . Table 1 summarizes the grid resolution studies at  $Re=8000$ . It shows the mean torque coefficients, averaged over a long time (typically about 100 inner-cylinder revolutions), on the inner and outer cylinder walls for different resolutions. The mean torque coefficient is defined as

$$C_T = \frac{\langle T \rangle}{0.5\pi\rho U_0^2 R_1^2 L_z} \quad (2.1)$$

where  $\langle T \rangle$  is the time-averaged torque on the cylinder walls. From case A to case G, the total degrees of freedom in the simulation have been increased 5-fold. The torque is observed to increase slightly and converge to its final value. A comparison among cases C to E (and between cases A and B) indicates that the mean torque coefficient is not very sensitive to the axial dimension of the domain (variation less

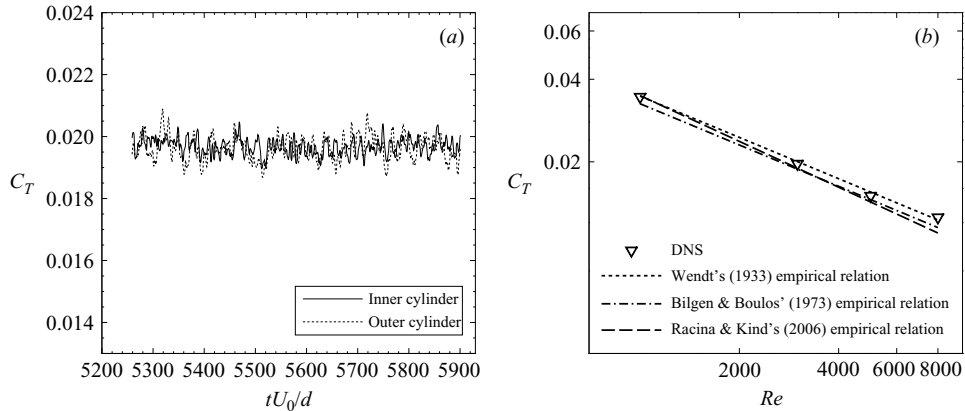


FIGURE 1. (a) Time history of instantaneous torque coefficients on inner and outer cylinder walls ( $Re = 3000$ ); torque values on the inner cylinder are made negative in the plot. (b) Comparison of mean torque coefficient as a function of Reynolds number between the present simulation and the experimental measurements of Wendt (1933), Bilgen & Boulos (1973) and Racina & Kind (2006).

than 1%). However, with a very large axial dimension (e.g. with an aspect ratio 16 or more) different flow states (with different wavelengths of the Taylor vortices) may be realized in the computations, as reported by Bilson & Bremhorst (2007), which is reminiscent of the non-unique flow states observed in experiments (Coles 1965; Koschmieder 1979). A consistent flow condition would be achieved with a shorter axial dimension (Bilson & Bremhorst 2007). Simulations at lower Reynolds numbers are mainly conducted with the same resolutions as case E and case G in table 1. We have performed long-time simulations of the flow at all Reynolds numbers considered. For each Reynolds number, after the flow reaches a statistically stationary state the statistical quantities are accumulated until convergence, which is typically averaged over about 300 convective time units ( $d/U_0$ ).

Figure 1(a) shows time histories of the instantaneous torque coefficients on the inner and outer cylinder walls at Reynolds number  $Re = 3000$ . The constancy of the mean demonstrates that the flow is statistically stationary while the small-scale rapid fluctuations are indicative of the highly unsteady nature of the flow. We have computed the mean torque coefficient for the four Reynolds numbers, and in figure 1(b) plotted it as a function of the Reynolds number. The empirical relations between torque and Reynolds number determined by Wendt (1933), Bilgen & Boulos (1973) and Racina & Kind (2006) for  $\eta = 0.5$  are also shown in the figure for comparison. Based on both Wendt (1933) and Bilgen & Boulos (1973), the torque scales as  $Re^{-0.5}$  for  $500 < Re < 10\,000$ , although with slightly different coefficients in the two empirical relations. Racina & Kind (2006) data, on the other hand, suggests a slightly different power scaling,  $Re^{-0.555}$ , for  $800 < Re < 10\,000$ . For Reynolds numbers ranging from 1000 to 8000, however, the differences among the three empirical relations are minor. Figure 1(b) demonstrates that the computed torque coefficients from the present simulation agree well with the experimental measurements, and appear to follow the  $Re^{-0.5}$  scaling more closely. Overall, the simulated results are in closest agreement with Wendt (1933) empirical relation.

In figure 2 we compare the profiles of the normalized mean angular momentum  $\langle ru_\theta \rangle / (R_1 U_0)$ , where  $u_\theta$  denotes the azimuthal velocity and  $r$  is the radial coordinate,

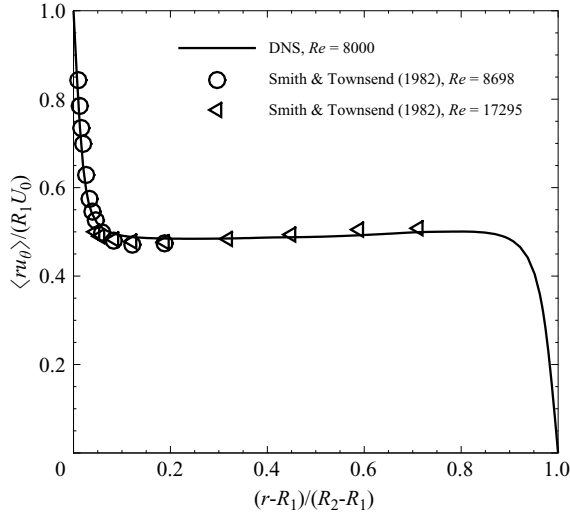


FIGURE 2. Comparison of normalized mean angular momentum profiles between present simulation ( $Re = 8000$ ) and the experiment of Smith & Townsend (1982).  $u_\theta$  is the azimuthal velocity.

between the present simulation at  $Re = 8000$  and the experiment of Smith & Townsend (1982). Smith & Townsend (1982) measured the mean angular momentum at several Reynolds numbers. The experimental data for the lowest Reynolds number,  $Re = 8698$ , in Smith & Townsend (1982) have been included in figure 2 for comparison. Because Smith & Townsend's (1982) data at this Reynolds number are available only for the region near the inner cylinder, in figure 2 we have also included data for the second lowest Reynolds number  $Re = 17295$  in the experiment for the middle region of the gap. The computed profile from the current simulation agrees with Smith & Townsend's (1982) data reasonably well. The result shows that the core of the flow ( $0.1 \lesssim (r - R_1)/(R_2 - R_1) \lesssim 0.9$ ) has an essentially constant mean angular momentum  $0.5R_1U_0$ , a phenomenon in turbulent Taylor–Couette flow also observed by Lewis & Swinney (1999) at higher Reynolds numbers. The computed angular momentum profile has a slightly positive slope in the core of the flow, consistent with the experimental measurement. However, this slope is slightly smaller than that from the experiment (figure 2). It should be noted that Smith & Townsend's (1982) data are at a radius ratio  $\eta = 0.667$  which is a little different from that in the current simulations ( $\eta = 0.5$ ). This difference is probably the cause of the slight difference in the slope of the profile between the simulation and the experiment.

### 3. Görtler vortices and herringbone streaks

In this section we investigate the flow structures in turbulent Taylor–Couette flow in detail. Emphasis is placed on the discussion of small-scale vortices near cylinder walls and the related effects. At each Reynolds number we monitor the signal of the torque on both cylinder walls (see figure 1a) during the simulation, and ensure that the flow has reached a statistically stationary state. All the results presented below are collected for statistically stationary states.

Figure 3 shows snapshots of instantaneous velocity fields in a radial–axial plane ( $r, z$  plane, where  $r$  is the radial coordinate), from left to right at Reynolds numbers

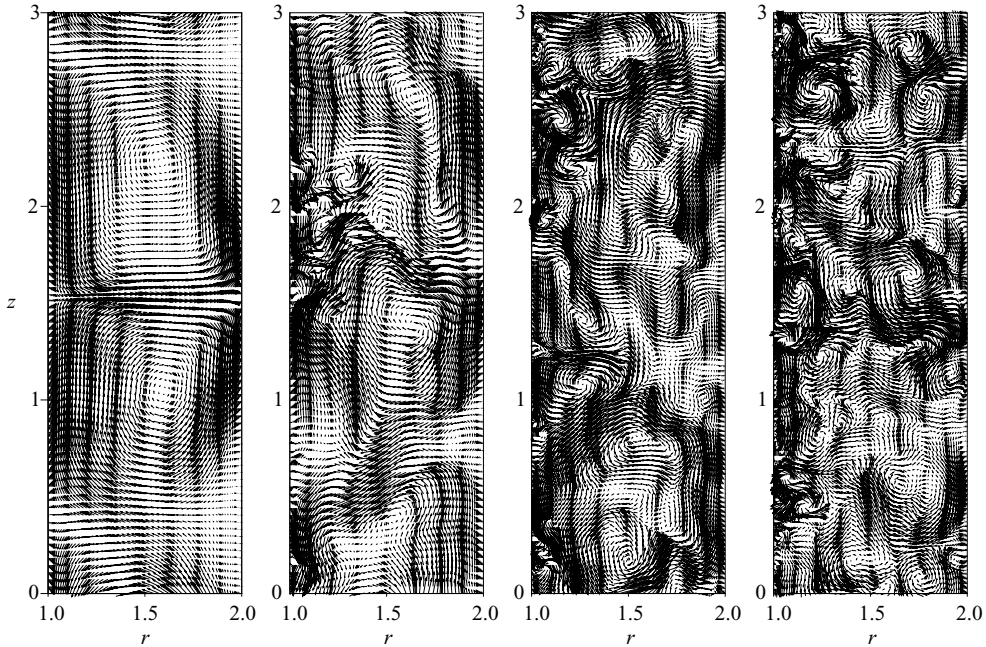


FIGURE 3. Instantaneous velocity fields in a radial–axial plane at Reynolds numbers (from left to right)  $Re = 1000, 3000, 5000$  and  $8000$ .

$Re = 1000, 3000, 5000$  and  $8000$  (a time-averaged flow field will be shown later in §4). Inner and outer cylinder walls correspond to  $r/d = 1.0$  and  $2.0$ , respectively. The velocity vectors have been plotted on the quadrature points of the spectral elements. The ‘stripes’ in the patterns are due to the non-uniform distribution of spectral elements in the radial direction (finer elements near both walls, coarser elements toward the middle of the gap) and the non-uniform distribution of quadrature points within an element (finer near element boundaries, coarser in the middle of an element). At  $Re = 1000$ , large-scale Taylor vortices are observed to occupy the entire gap, with well-defined inflow and outflow boundaries between the vortex cells. As the Reynolds number increases to  $3000$ , the Taylor vortices become severely distorted. Although not as well-defined as at  $Re = 1000$ , a Taylor vortex cell can still be clearly identified, with some cells consisting of two or more smaller vortices rotating in contiguous directions. In addition, azimuthal vortices with scales significantly smaller than the Taylor vortex, Görtler vortices, emerge on the inner cylinder wall around distorted outflow boundaries of the Taylor vortex cells. These vortices are absent from the outer cylinder wall at this Reynolds number.

At  $Re = 5000$ , the core of the flow is characterized by the presence of a number of vortices, apparently randomly distributed and with scales significantly smaller than the gap width. It is not obvious how to identify a large-scale Taylor vortex in this case. Based on the sense of rotation of vortices, large-scale ‘Taylor cells’, each encompassing a pack of vortices, may be vaguely recognized, but the ‘boundaries’ between cells are highly distorted and in some cases interrupted by vortices near the wall. The number of small-scale vortices near the inner cylinder increases, and they generate energetic fluid motions normal to the wall. Although these near-wall vortices appear to concentrate on the highly distorted outflow boundaries between ‘Taylor cells’, they are also observed in other regions of the wall such as near the inflow

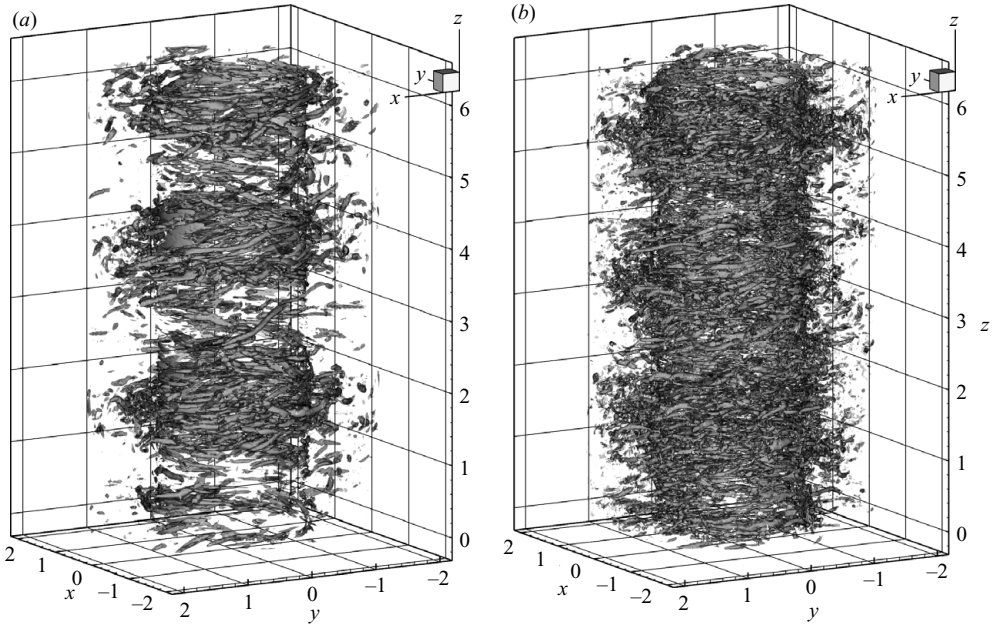


FIGURE 4. Iso-surfaces of instantaneous  $\lambda_2$ , the intermediate eigenvalue in the vortex identification method by Jeong & Hussain (1995): (a)  $Re = 5000$  and (b)  $Re = 8000$ . Two levels are shown corresponding to  $\lambda_2 = -2$  and  $-3.5$ .

boundaries. Such small-scale vortices can be observed near the outer cylinder wall as well at this Reynolds number.

As the Reynolds number increases to  $Re = 8000$ , the flow core teems with vortices, and large-scale ‘Taylor cells’ can hardly be distinguished from the instantaneous velocity field. A large number of small-scale vortices can be observed near the inner cylinder, appearing randomly distributed on the wall. The number of small-scale vortices near the outer cylinder has also increased, although it is notably smaller than at the inner cylinder wall.

The above observation concerning the onset of small-scale Görtler vortices is consistent with the previous studies. Although Barcion *et al.* (1979) first hypothesized the existence of Görtler vortices after observing near-wall herringbone-like streaks, it was Wei *et al.* (1992) who demonstrated that Görtler vortices appeared first at the inner cylinder wall with increasing Reynolds number. The present results have confirmed Wei *et al.* (1992) observation. The simulation has further suggested that these vortices appear first around the outflow boundaries (figure 3). These observations support the instability analyses of Coughlin & Marcus (1992*b*) and Vastano & Moser (1991), who suggested that the outflow boundary jets between the Taylor vortices were the most unstable regions in the flow.

To explore the structural characteristics of the near-wall Görtler vortices in three-dimensional space, we plot in figure 4 the iso-surfaces of  $\lambda_2$ , the intermediate eigenvalue of the tensor  $\mathbf{S}:\mathbf{S} + \mathbf{\Omega}:\mathbf{\Omega}$  (where  $\mathbf{S}$  and  $\mathbf{\Omega}$  are the symmetric and antisymmetric parts of the velocity gradient respectively) in Jeong & Hussain (1995), and in Figure 5 the iso-surfaces of the instantaneous pressure (near the inner cylinder wall), for  $Re = 5000$  and  $8000$ . A forest of small-scale vortical structures can be clearly observed in the flow, extending along the azimuthal direction. At  $Re = 5000$ ,

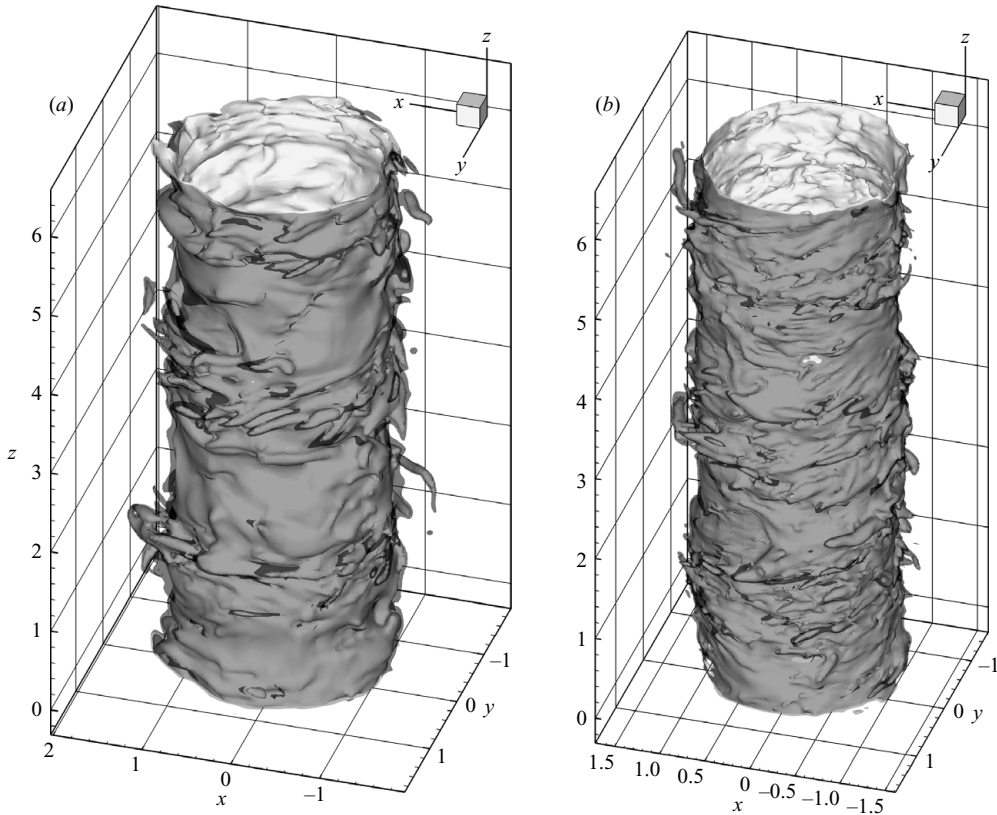


FIGURE 5. Iso-surfaces of instantaneous pressure: (a)  $Re = 5000$ ,  $p/(\rho U_0^2) = -0.045$  and  $-0.04$ . (b)  $Re = 8000$ ,  $p/(\rho U_0^2) = -0.02$  and  $-0.025$ .

the vortices exhibit an uneven distribution in the axial direction. They are observed to concentrate in several axially banded regions encircling the cylinder, corresponding to the outflow boundaries between the Taylor cells. Instantaneously, these vortices appear to originate from the wall, stretch azimuthally and extend away from the wall. Careful examination shows that the orientations of these vortices are not in the planes perpendicular to the  $z$ -axis. The majority are oriented at a small angle with respect to the  $(x, y)$ -plane. Similar observations can be made for  $Re = 8000$ . However, at  $Re = 8000$  there appears to be a larger population of vortices and they are more randomly distributed in the axial direction, unlike the lower Reynolds number. The vortices are also not as azimuthally stretched as at  $Re = 5000$ , and therefore tend to appear ‘shorter’.

The vortices observed here bear some resemblance to the quasi-streamwise vortices in turbulent channel flows. By extracting the coherent structures in a turbulent channel flow with a conditional sampling technique, Jeong *et al.* (1997) showed that the dominant near-wall structures were elongated quasi-streamwise vortices that overlapped in the streamwise direction as a staggered array. These overlapping vortices were inclined in the streamwise–wall-normal planes and tilted in the streamwise–spanwise planes. Recently, Jimenez and co-workers (del Alamo *et al.* 2006) also reported the presence of wall-attached vortex clusters in turbulent channel flow at high Reynolds numbers. They observed that these clusters were usually inclined upward (away from wall) and along the streamwise direction.

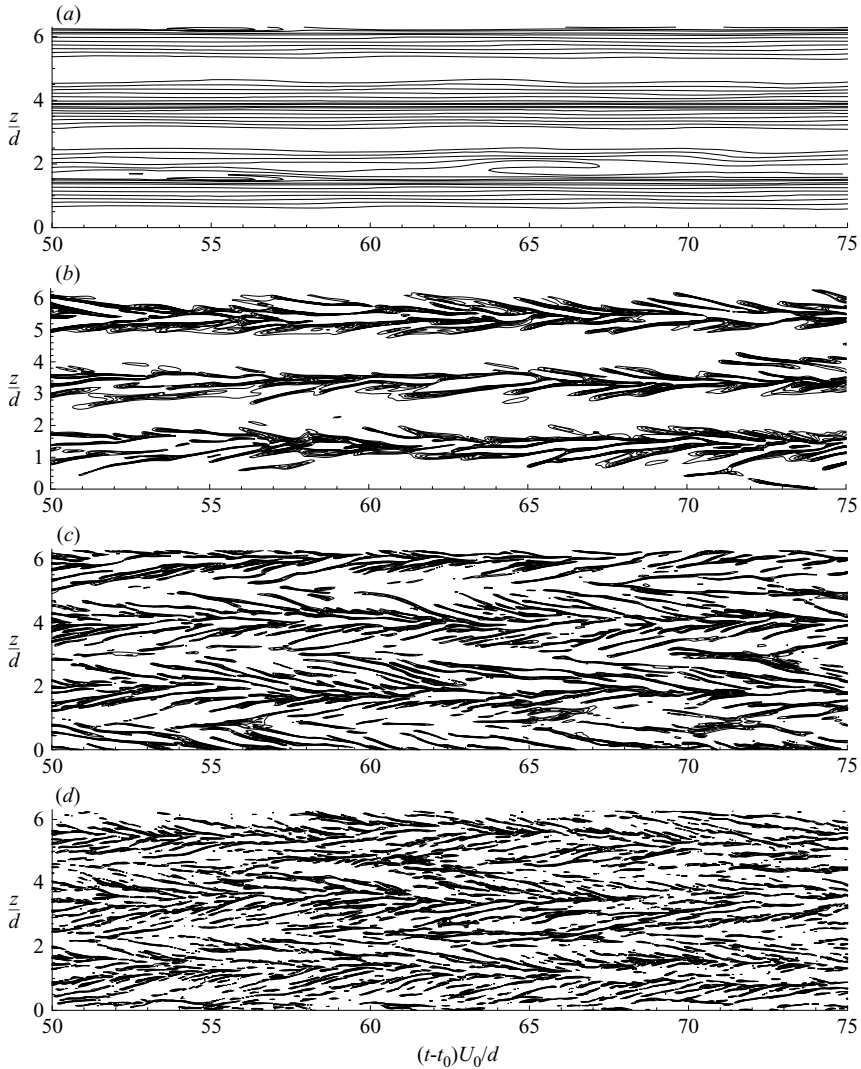


FIGURE 6. Herringbone-like streaks demonstrated by spatial-temporal plots of the azimuthal velocity along a fixed line oriented in the  $z$ -direction a distance  $0.033d$  away from the inner cylinder wall. Shown are azimuthal velocity contours at 8 equi-levels between  $0.65U_0$  and  $0.9U_0$  for (a)  $Re = 1000$ , (b)  $Re = 3000$ , (c)  $Re = 5000$ , (d)  $Re = 8000$ .

Figure 6 demonstrates the spatial-temporal characteristics of the azimuthal velocity. The velocity data were collected along a fixed line oriented in the  $z$ -direction and located near the inner cylinder wall (at a distance  $0.033d$ ). Shown are the instantaneous azimuthal velocity contours in the spatial-temporal  $(t, z)$ -plane for Reynolds numbers from  $Re = 1000$  to  $8000$ , with  $u_\theta/U_0|_{min} = 0.65$ ,  $u_\theta/U_0|_{max} = 0.9$  and an increment  $\Delta u_\theta/U_0 = 0.0357$  between contour levels. At  $Re = 1000$ , the contour lines are clustered around axial locations that coincide with the outflow boundaries between Taylor vortex cells, indicative of persistent high azimuthal velocity values in those regions. Localized ‘defects’ can be observed in the distribution, indicating occasional disturbances to the flow that die down over time. For Reynolds numbers  $Re = 3000$  and above, intriguing herringbone-like patterns of streaks can be observed

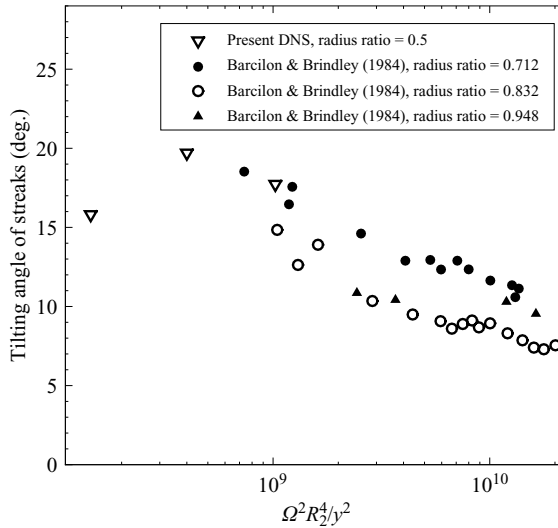


FIGURE 7. Average tilting angle of herringbone streaks from the present DNS and Barcilon & Brindley's (1984). Note that the  $x$ -axis is  $\Omega^2 R_2^4 / \nu^2$ , as prescribed by Barcilon & Brindley (1984).

in the distribution, reminiscent of the flow photographs of Barcilon *et al.* (1979). At  $Re = 3000$ , the herringbone streaks are distributed in disjoint bands around the outflow boundaries of the Taylor cells, providing additional evidence of the concentration of Görtler vortices in those regions. At  $Re = 5000$ , we observe a considerable increase in the population of streaks compared to  $Re = 3000$ , and the spacing between neighbouring streaks appears to be substantially decreased. Although the concentration of streaks around the outflow boundaries is still quite clear from the banded distribution pattern, adjacent bands of streaks are not completely disjoint. In fact, streaks from neighbouring bands are observed to intersect and become entangled on occasions. As the Reynolds number reaches  $Re = 8000$ , the herringbone streaks become significantly finer and more closely packed, and the population has dramatically increased. The streaks become less coherent in that more appear broken, shorter, and scattered. Although the banded pattern may still be vaguely discerned, the bands meander in the axial direction over time and the streaks appear to be randomly distributed.

The tilting angles of the herringbone streaks have been computed for these Reynolds numbers. Assume the flow travels at a mean azimuthal velocity  $U_\theta(r_l)$  at the location of the fixed line, where  $r_l = R_1 + 0.033d$  is the radial coordinate of the line. The mean azimuthal velocity  $U_\theta(r_l)$  is available from the flow statistics (see §4). In the spatial–temporal plots of figure 6, a time interval  $\Delta t$  is therefore equivalent to a distance  $U_\theta(r_l)\Delta t$  based on the Taylor hypothesis, and the tilting angle can be evaluated as a result. In figure 7 we plot the average magnitude of the tilting angle of the herringbone streaks as a function of  $\Omega^2 R_2^4 / \nu^2 = Re^2 / [\eta^2(1 - \eta)^2]$ , a characteristic Reynolds number prescribed by Barcilon & Brindley (1984), for Reynolds numbers from 3000 to 8000. The figure includes results from the present DNS ( $\eta = 0.5$ ) and the data from Barcilon & Brindley (1984) for  $\eta = 0.712, 0.832$  and  $0.948$ . The data points from the simulations lie at the lower end in terms of  $\Omega^2 R_2^4 / \nu^2$ , and they generally follow the trend of Barcilon & Brindley's (1984) data, which suggests an increase in the tilting angle as  $\Omega^2 R_2^4 / \nu^2$  decreases. The observed tilting angle at  $Re = 3000$  is somewhat lower than at  $Re = 5000$  from the present simulation. One possibility is that

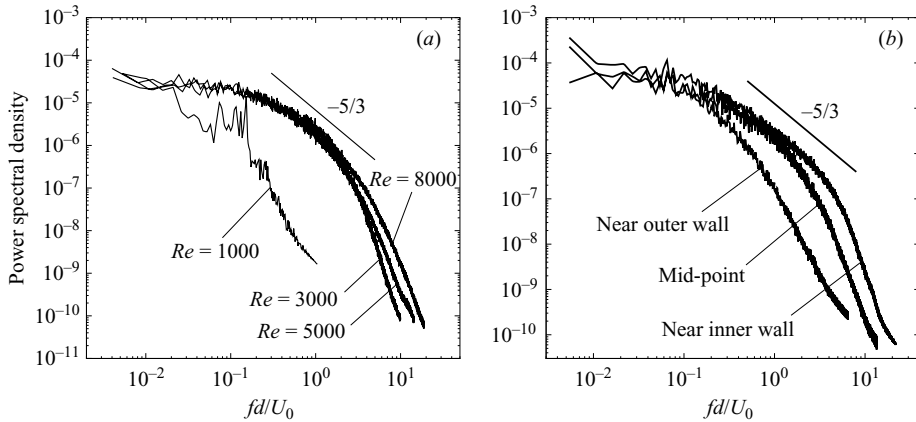


FIGURE 8. Velocity power spectra. (a) Temporal power spectra of the azimuthal velocity at a distance  $0.108d$  from the inner cylinder wall for different Reynolds numbers. (b) Power spectra of the axial velocity in the middle of the gap, and at two other locations at distance  $0.033d$  from the inner and outer cylinder walls, respectively, for  $Re = 8000$ .

with decreasing Reynolds number the tilting angle may reach a peak value at some point and then decrease as the Reynolds number further decreases, since at sufficiently low Reynolds numbers the herringbone streaks will disappear, as demonstrated by figure 6(a) for  $Re = 1000$  in the present simulation and by the flow photographs at low Taylor numbers in Barcilon *et al.* (1979).

We next investigate the spectral characteristics of turbulent fluctuations in Taylor–Couette flow. Figure 8(a) shows a comparison of the temporal power spectra of the azimuthal velocity at a distance  $0.108d$  from the inner cylinder wall for Reynolds numbers  $Re = 1000, 3000, 5000$  and  $8000$ . Velocity power spectra are computed based on the time histories of the velocity at ‘history points’, and are averaged over the points along the axial direction with the same radial and azimuthal coordinates. Compared to higher Reynolds numbers, the spectrum at  $Re = 1000$  lacks significant high-frequency components, with negligible spectral density beyond the peak frequency, indicating that the flow remains laminar at this Reynolds number. In contrast, the power spectra at  $Re = 3000, 5000$  and  $8000$  all exhibit a broadband distribution which is characteristic of a turbulent power spectrum, demonstrating that the flow has become turbulent at these Reynolds numbers. The power spectrum curves of these three Reynolds numbers essentially collapse onto one at low frequencies ( $fd/U_0 \lesssim 2$ ). At high frequencies, the larger the Reynolds number, the higher the power spectral density, suggesting more energetic turbulent fluctuations with increasing Reynolds numbers.

In figure 8(b) we compare the power spectra of the axial velocity at  $Re = 8000$  at three locations: near the inner cylinder wall (at a distance  $0.033d$ ), in the middle of the gap, and near the outer cylinder wall (at a distance  $0.033d$ ). Velocity spectra have been averaged over points along the axial direction with the same radial and azimuthal coordinates. Increasingly stronger high-frequency components are observed in the power spectra with decreasing radial coordinates, indicating an uneven distribution of the intensity of turbulent fluctuations. More energetic turbulent fluctuations are observed toward the inner cylinder wall. The velocity spectra at  $Re = 3000$  and  $5000$  possess similar characteristics. This demonstrates that turbulence at the inner cylinder wall is substantially stronger than at the outer cylinder in turbulent

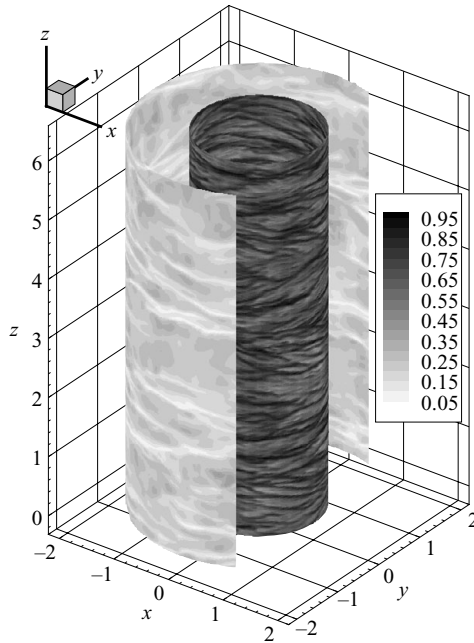


FIGURE 9. Contours of instantaneous azimuthal velocity on two near-wall grid surfaces (nearly cylindrical) showing the high-speed streaks on the inner cylinder and low-speed streaks on the outer cylinder ( $Re = 8000$ ).

Taylor–Couette flow. Note that in the configuration studied in this paper, the inner cylinder rotates while the outer cylinder is stationary. Although in plane Couette flow only the difference between velocities at the two walls is significant, this is not the case in Taylor–Couette flow. The curvature effect causes the asymmetry in the intensity distribution of turbulent fluctuations.

Streaky structures in near-wall regions are common characteristics of wall-bounded turbulence. In turbulent Taylor–Couette flow the inner cylinder wall teems with high-speed streaks while the outer cylinder wall teems with low-speed streaks. In figure 9 we plot contours of the instantaneous azimuthal velocity on two grid surfaces (nearly cylindrical) near the inner and outer cylinder walls at  $Re = 8000$ . Numerous azimuthally elongated streaks with higher azimuthal velocities (high-speed streaks) can be observed on the inner cylinder wall, while on the outer cylinder wall the azimuthal velocity in these streaky regions is lower (low-speed streaks) and the streaks are considerably fewer. Visually, these streaks are not dissimilar to the near-wall ‘low-speed streaks’ observed in other turbulent flows in simpler geometries such as a channel. Close examination of the high-speed streaks on the inner cylinder and the low-speed streaks on the outer cylinder, however, reveals their intricate herringbone-like pattern, which is absent from those in turbulent channel flows.

In order to determine the axial spacings of the high-speed and low-speed streaks on the cylinder walls, we examine the spatial power spectrum of the velocity. The spatial spectrum is obtained by computing the spatial FFT of the velocity data along a line oriented in the axial direction. Figure 10(a) shows the time-averaged spatial power spectrum of the radial velocity at a line adjacent to the inner cylinder wall (at a distance  $0.033d$ ) at  $Re = 8000$ . The wavenumber at the sharp peak,  $k_{Taylor}$ , is indicative of the spacing of Taylor cells. In this case it corresponds to three pairs of Taylor

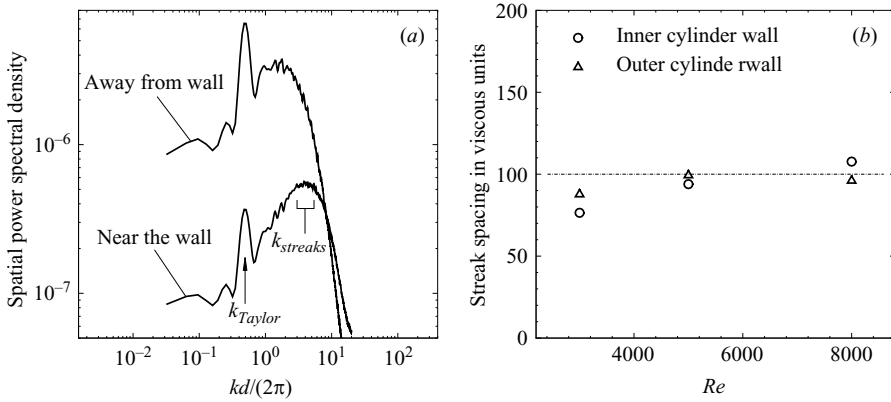


FIGURE 10. Streak spacings. (a) Spatial power spectrum of the radial velocity ( $Re = 8000$ ), where  $k$  is the wavenumber. (b) Axial spacings of streaks in viscous wall units as a function of the Reynolds number.

vortex cells for a domain with axial dimension  $L_z/d = 2\pi$ , as shown by the mean flow in §4. In addition, a prominent broadband peak can be observed in the spectrum at high wavenumbers, corresponding to the streaks on the wall. The broadband nature of the peak suggests that the streak spacing varies within a range. This broadband peak has a higher power spectral density than the sharp peak at  $k_{Taylor}$ , indicative of the dominance of small-scale vortices near the wall. For comparison, we also show the axial spectrum at a line away from the inner cylinder wall (at a distance  $0.108d$ ) in figure 10(a). The sharp peak at  $k_{Taylor}$  is notably stronger (in terms of spectral density) than the broadband peak, contrary to the case near the wall, which suggests the dominance of motions at scales of Taylor vortices away from the wall. Compared to the near-wall spectrum, the broadband peak has moved toward lower wavenumbers. This indicates an increase in the streak spacing away from the wall, which is consistent with observations in previous studies of turbulent channel flows and boundary layers (Smith & Metzler 1983; Kim, Moin & Moser 1987; Rashidi & Banerjee 1990). To determine the streak spacing near the wall, we use the average wavenumber at the broadband peak of the near-wall spectrum.

Figure 10(b) shows the streak spacings on the inner and outer cylinder walls, in viscous wall units, as a function of the Reynolds number. They have been normalized by  $v/u_\tau$ , where  $u_\tau$  is the friction velocity at the inner and outer cylinder walls. At  $Re = 5000$  and  $8000$ , the streak spacing on both inner and outer cylinders is approximately 100 viscous wall units, the same as that in turbulent channel flows which have been investigated in numerous previous studies (see e.g. Kline *et al.* 1967). At  $Re = 3000$  the normalized streak spacing is somewhat smaller, probably due to the relatively weak turbulence at this Reynolds number (see figure 8a). Since the viscous wall unit decreases as Reynolds number increases, the scale of the azimuthal vortices and wall streaks would become smaller at higher Reynolds numbers.

#### 4. Statistical characteristics

We investigate the statistical characteristics of turbulent Taylor–Couette flow in this section. Figure 11 compares the flow patterns in a radial–axial ( $r, z$ ) plane of an instantaneous snapshot and of the mean velocity field at  $Re = 8000$ . The instantaneous flow field teems with small-scale azimuthal vortices, and the Taylor vortex cells are by

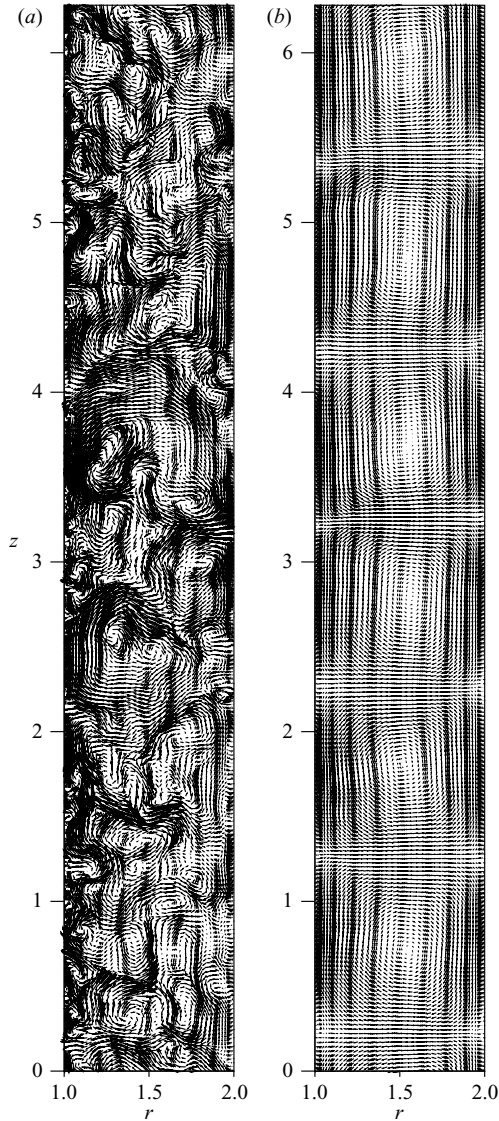


FIGURE 11. Comparison of (a) instantaneous and (b) time-averaged mean flow patterns in a radial-axial plane at  $Re = 8000$ .

no means clear from the instantaneous velocity patterns (see also figure 3). The time-averaged mean velocity field, on the other hand, reveals the presence of organized Taylor vortex cells underlying turbulent fluctuations (figure 11*b*). Instantaneously, turbulent fluctuations are superimposed on these organized Taylor vortices, distorting and interrupting the inflow/outflow boundaries. As the Reynolds number increases, the underlying Taylor vortices are overwhelmed by the turbulent fluctuations in the instantaneous flow. These mean characteristics are consistent with the turbulent toroidal eddies observed in previous flow visualizations and experiments (Koschmieder 1979; Smith & Townsend 1982; Townsend 1984). The signature of these underlying Taylor vortex cells can also be seen in the spatial velocity spectrum (figure 10*a*) and in the patterns of herringbone-like streaks.

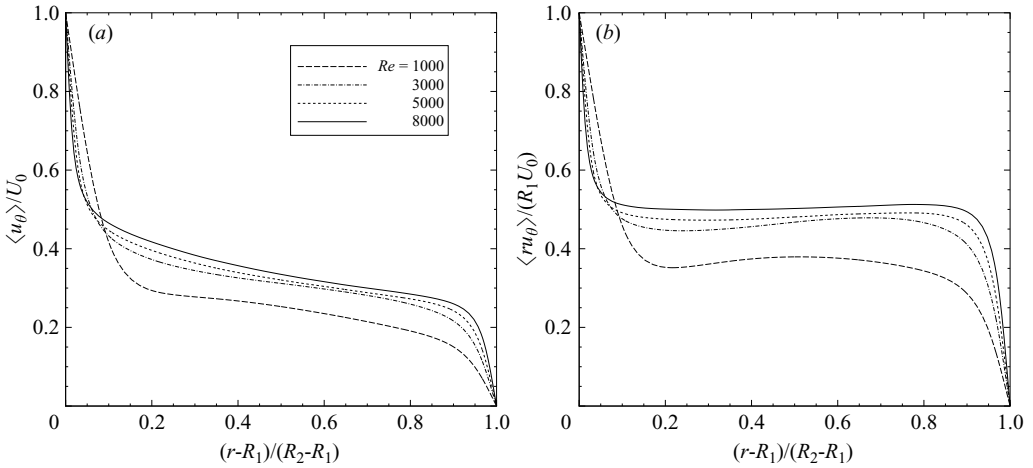


FIGURE 12. Comparison of (a) mean velocity and (b) mean angular momentum profiles of different Reynolds numbers.

In figure 12 we compare profiles of the mean azimuthal velocity and the mean angular momentum of different Reynolds numbers, which have been averaged over time and also along the axial direction. The mean velocity has been normalized by the rotation velocity of the inner cylinder,  $U_0$ , and the mean momentum by  $R_1 U_0$ . Note the asymmetry of the mean velocity profiles at the inner and outer cylinder walls, unlike plane Couette flows. An increase in the Reynolds number results in higher velocity gradients at both cylinder walls and larger azimuthal velocities in the flow core, as shown by figure 12(a). Figure 12(b) compares the mean angular momentum profiles at the four Reynolds numbers. As demonstrated by the velocity spectra (figure 8a), the flow is laminar at  $Re = 1000$  and becomes turbulent at Reynolds numbers  $Re = 3000$  and above. Turbulent flows exhibit an essentially constant mean angular momentum in the core (see also Smith & Townsend 1982 and Dubrulle *et al.* 2005). For the laminar flow at  $Re = 1000$  the mean angular momentum is close to a constant in the middle region of the gap, but there is a notable variation in the profile. With increasing Reynolds number the region with constant angular momentum becomes larger, occupying approximately 80% of the gap width at  $Re = 8000$ . A comparison between  $Re = 1000$  and  $Re = 3000$  indicates that there is a substantial increase in the angular momentum of the core as the flow transitions from laminar to turbulent states. On the other hand, the mean angular momentum in the core increases only slightly with increasing Reynolds number once the flow becomes turbulent. The bulk angular momentum is about  $0.5 R_1 U_0$  at  $Re = 8000$ . Lewis & Swinney (1999) measured the angular momentum in the core of the flow for a radius ratio  $\eta = 0.724$  at Reynolds numbers between  $Re = 1.2 \times 10^4$  and  $5.4 \times 10^5$ , and concluded that to good approximation it was a constant given by  $0.5 R_1 U_0$ . The present simulation results are consistent with their measurement.

Figure 13 compares profiles of the root-mean-square (r.m.s.) azimuthal fluctuation velocity (normalized by  $U_0$ ) at different Reynolds numbers. The double peaks in the profiles suggest stronger velocity fluctuations near both cylinder walls, which is analogous to those observed in turbulent channel flows (Moser & Moin 1987). The inner peak is substantially higher than the outer one, indicating that the most

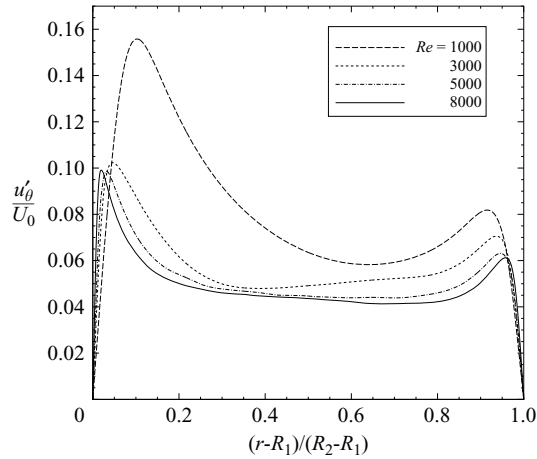


FIGURE 13. Comparison of r.m.s. azimuthal fluctuation velocity profiles of different Reynolds numbers.

energetic turbulence occurs near the inner cylinder wall. The two peaks in the r.m.s. velocity profiles move closer to both cylinder walls with increasing Reynolds number.

## 5. Concluding remarks

In this paper we have studied turbulent Taylor–Couette flow at Reynolds numbers ranging from 1000 to 8000 for a radius ratio  $\eta = 0.5$  employing detailed three-dimensional direct numerical simulations. We have focused on the dynamics of small-scale Görtler vortices and the herringbone-like streaks near both cylinder walls, and the statistical features of Taylor–Couette turbulence.

Barcilon *et al.* (1979) first reported observations of small-scale structures near cylinder walls that formed a fine herringbone-like pattern of streaks in Taylor–Couette experiments. They conjectured that these streaks were the inflow/outflow boundaries of Görtler vortices, which were due to a centrifugal instability, occurring in a curved flow in which the local angular momentum decreased outwards along the radius of curvature (Saric 1994). This elementary theory was compared with experiments, and good agreement was observed. Subsequently, Barcilon & Brindley (1984) developed a mathematical formulation to model the system of Taylor and Görtler vortices hypothesized in Barcilon *et al.* (1979), exploiting the separation of scales of the Taylor mode (commensurate with the gap width) and the Görtler mode (commensurate with the boundary layer thickness) and the assumption of ‘marginal stability’ (see Barcilon *et al.* 1979). The results of this model were shown to be in good agreement with a number of features of experimental observations. Wei *et al.* (1992) critically evaluated the Görtler hypothesis of Barcilon *et al.* (1979) and Barcilon & Brindley (1984) with detailed experiments for a wide range of radius ratios and Reynolds numbers. They noted that the radius of curvature and the velocity gradient were the crucial parameters governing the strength of the Görtler mechanism. The combination of a smaller radius of curvature and a larger velocity gradient at the inner cylinder (compared to the outer one) therefore suggested the emergence of Görtler vortices at the inner cylinder wall before the outer cylinder. With flow visualizations, they indeed observed that Görtler vortices appeared first at the inner cylinder wall,

and at a Taylor number an order of magnitude lower than those reported by Barcilon *et al.* (1979).

Results of the present simulations have confirmed the above experimental observations of the near-wall herringbone streaks and the onset of Görtler vortices at the inner cylinder wall. Furthermore, the simulations have revealed additional characteristics. We observe that the Görtler vortices originate around the outflow boundaries between Taylor vortex cells. In three-dimensional space these vortices are distributed randomly in banded regions concentrating at the outflow boundaries. With increasing Reynolds number they spread over the entire cylinder surface, and their concentration around the outflow boundaries becomes less obvious. Instantaneously, a Görtler vortex appears to originate from the wall, stretch azimuthally, and extend away from the wall.

When studying the transition to turbulence in Taylor–Couette flow, Townsend and co-workers (Smith & Townsend 1982; Townsend 1984) presented arguments that at moderately high Reynolds numbers Görtler vortices dominated the near-wall structure, and as the Reynolds number increased further the near-wall structure became more like that of a plane turbulent boundary layer. This implies a distinct difference between Görtler vortices and the structures of plane turbulent boundary layers which are dominated by quasi-streamwise vortices near the wall (Robinson 1991; Jeong *et al.* 1997). Wei *et al.* (1992) noted that this assumption was in conflict with the work of Blackwelder (see e.g. Swearingen & Blackwelder 1987) who argued that the near-wall streamwise vortices found in plane turbulent boundary layers may be created by the Görtler mechanism due to the curvature of small surface imperfections present in physical experiments. The near-wall azimuthal vortices observed in the present simulations are not dissimilar to the near-wall streamwise vortices observed in plane turbulent channel flows. For example, both result in stronger r.m.s. velocity fluctuations (figure 13) and the streaky structures near the wall. While the near-wall streaks in turbulent Taylor–Couette flow form herringbone patterns, the average streak spacing is about 100 viscous wall units (figure 10*b*) in both types of flows.

We summarize the main results of this study as follows:

(i) Görtler vortices originate from the outflow boundaries between Taylor vortex cells at the inner cylinder wall.

(ii) In three-dimensional space Görtler vortices are randomly distributed in banded regions on the wall, concentrating at the outflow boundaries. With increasing Reynolds number these vortices spread over the entire cylinder surface.

(iii) Görtler vortices cause near-wall streaky structures that form herringbone-like patterns. The average axial spacing of these streaks is approximately 100 viscous wall units. The tilting angle of the streaks approximately ranges from 16 to 20° in the range of Reynolds numbers studied here.

(iv) The mean angular momentum is essentially a constant in the core of turbulent Taylor–Couette flow. The value of this constant increases slightly with increasing Reynolds number in the range of turbulent Reynolds numbers in this study. It is approximately  $0.5R_1^2\Omega$  in the core at the highest Reynolds number studied here,  $Re = 8000$ .

(v) The mean velocity field reveals organized Taylor vortices underlying the turbulent Taylor–Couette flow. The instantaneous flow is a superposition of turbulent fluctuations on these organized Taylor vortices.

The author gratefully acknowledges the support from the National Science Foundation (NSF). Computer time was provided by the TeraGrid (TACC, NCSA,

SDSC, PSC) through an MRAC grant, and by the Rosen Center for Advanced Computing (RCAC) at Purdue University.

## REFERENCES

- DEL ALAMO, J. C., JIMENEZ, J., ZANDONADE, P. & MOSER, R. D. 2006 Self-similar vortex clusters in the turbulent logarithmic region. *J. Fluid Mech.* **561**, 329–358.
- BARCILON, A. & BRINDLEY, J. 1984 Organized structures in turbulent Taylor–Couette flow. *J. Fluid Mech.* **143**, 429–449.
- BARCILON, A., BRINDLEY, J., LESSEN, M. & MOBBS, F. R. 1979 Marginal instability in Taylor–Couette flows at a high Taylor number. *J. Fluid Mech.* **94**, 453–463.
- BARENGHI, C. F. & JONES, C. A. 1989 Modulated Taylor–Couette flow. *J. Fluid Mech.* **208**, 127–160.
- BATTEN, W. M., BRESSLOFF, N. W. & TURNOCK, S. R. 2002 Transition from vortex to wall driven turbulence production in the Taylor–Couette system with a rotating inner cylinder. *Intl J. Numer. Method Fluids* **38**, 207–226.
- VAN DEN BERG, T. H., DOERING, C. R., LOHSE, D. & LATHROP, D. P. 2003 Smooth and rough boundaries in turbulent Taylor–Couette flow. *Phys. Rev. E* **68**, 036307.
- BILGEN, E. & BOULOS, E. 1973 Functional dependence of torque coefficient of coaxial cylinders gap width and reynolds numbers. *Trans. ASME: J. Fluids Engng* **95**, 122–126.
- BILSON, M. & BREMHORST, K. 2007 Direct numerical simulation of turbulent Taylor–Couette flow. *J. Fluid Mech.* **579**, 227–270.
- BRANDSTATER, A. & SWINNEY, H. L. 1987 Strange attractors in weakly turbulent Couette–Taylor flow. *Phys. Rev. A* **35**, 2207–2220.
- CLIFFE, K. A. & MULLIN, T. 1985 A numerical and experimental study of anomalous modes in the Taylor experiment. *J. Fluid Mech.* **153**, 243–258.
- COLES, D. 1965 Transition in circular Couette flow. *J. Fluid Mech.* **21**, 385–425.
- COUGHLIN, K. T. & MARCUS, P. S. 1992a Modulated waves in Taylor–Couette flow Part 1. analysis. *J. Fluid Mech.* **234**, 1–18.
- COUGHLIN, K. T. & MARCUS, P. S. 1992b Modulated waves in Taylor–Couette flow Part 2. numerical simulation. *J. Fluid Mech.* **234**, 19–46.
- COUGHLIN, K. & MARCUS, P. S. 1996 Turbulent bursts in Couette–Taylor flow. *Phys. Rev. Lett.* **77**, 2214–2217.
- COUGHLIN, K. T., MARCUS, P. S., TAGG, R. P. & SWINNEY, H. L. 1991 Distinct quasiperiodic modes with like symmetry in a rotating fluid. *Phys. Rev. Lett.* **66**, 1161–1164.
- CZARNY, O., SERRE, E., BONToux, P. & LUEPTOW, R. M. 2004 Interaction of wavy cylindrical Couette flow with endwalls. *Phys. Fluids* **16**, 1140–1148.
- DI PRIMA, R. C. & SWINNEY, H. L. 1981 Instabilities and transition in flow between concentric rotating cylinders. In *Hydrodynamic Instabilities and the Transition to Turbulence* (ed. H. L. Swinney & J. P. Gollub) pp. 139–180. Springer.
- DONG, S. & KARNIADAKIS, G. E. 2005 DNS of flow past a stationary and oscillating cylinder at  $Re = 10000$ . *J. Fluids Struct.* **20**, 519–531.
- DONG, S., KARNIADAKIS, G. E., EKMEKCI, A. & ROCKWELL, D. 2006 A combined direct numerical simulation–particle image velocimetry study of the turbulent near wake. *J. Fluid Mech.* **569**, 185–207.
- DONNELLY, R. J. & SIMON, N. J. 1959 An empirical torque relation for supercritical flow between rotating cylinders. *J. Fluid Mech.* **7**, 401–418.
- DUBRULLE, B., DAUCHOT, O., DAVIAUD, F., LONGARETTI, P.-Y., RICHARD, D. & ZAHN, J.-P. 2005 Stability and turbulent transport in Taylor–Couette flow from analysis of experimental data. *Phys. Fluids* **17**, 095103.
- FASEL, H. & BOOZ, O. 1984 Numerical investigation of supercritical Taylor–vortex flow for a wide gap. *J. Fluid Mech.* **138**, 21–52.
- FERNSTERMATHER, P. R., SWINNEY, H. L. & GOLLUB, J. P. 1979 Dynamical instabilities and the transition to chaotic Taylor vortex flow. *J. Fluid Mech.* **94**, 103–128.
- GÖRTLER, H. 1954 On the three-dimensional instability of laminar boundary layers on concave walls. *NACA TM* 1375.
- JEONG, J. & HUSSAIN, F. 1995 On the identification of a vortex. *J. Fluid Mech.* **285**, 69–94.

- JEONG, J., HUSSAIN, F., SCHOPPA, W. & KIM, J. 1997 Coherent structures near the wall in a turbulent channel flow. *J. Fluid Mech.* **332**, 185–214.
- JONES, C. A. 1981 Nonlinear Taylor vortices and their stability. *J. Fluid Mech.* **102**, 249–261.
- JONES, C. A. 1982 On flow between counter-rotating cylinders. *J. Fluid Mech.* **120**, 433–450.
- JONES, C. A. 1985 The transition to wavy Taylor vortices. *J. Fluid Mech.* **157**, 135–162.
- KARNIADAKIS, G. E., ISRAELI, M. & ORSZAG, S. A. 1991 High-order splitting methods for the incompressible Navier-Stokes equations. *J. Comput. Phys.* **97**, 414–443.
- KARNIADAKIS, G. E. & SHERWIN, S. J. 2005 *Spectral/hp Element Methods for Computational Fluid Dynamics*, 2nd edn. Oxford University Press.
- KIM, J., MOIN, P. & MOSER, R. 1987 Turbulent statistics in fully-developed channel flow at low reynolds-number. *J. Fluid Mech.* **177**, 133–166.
- KING, G. P., LI, Y., LEE, W., SWINEY, H. L. & MARCUS, P. S. 1984 Wave speeds in wavy Taylor-vortex flow. *J. Fluid Mech.* **141**, 365–390.
- KIRBY, R. M. & KARNIADAKIS, G. E. 2003 De-aliasing on non-uniform grids: algorithms and applications. *J. Comput. Phys.* **91**, 249–264.
- KLINE, S. J., REYNOLDS, W.C., SCHRAUB, F. A. & RUNSTADLER, P. W. 1967 The structure of turbulent boundary layers. *J. Fluid Mech.* **30**, 741.
- KOSCHMIEDER, E. L. 1979 Turbulent Taylor vortex flow. *J. Fluid Mech.* **93**, 515–527.
- LATHROP, D. P., FINEBERG, J. & SWINNEY, H. L. 1992a Transition to shear-driven turbulence in Couette-Taylor flow. *Phys. Rev. A* **46**, 6390–6405.
- LATHROP, D. P., FINEBERG, J. & SWINNEY, H. L. 1992b Turbulent flow between concentric rotating cylinders at large reynolds number. *Phys. Rev. Lett.* **68**, 1515–1518.
- LEWIS, G. S. & SWINNEY, H. L. 1999 Velocity structure functions, scaling, and transitions in high-Reynolds-number Couette-Taylor flow. *Phys. Rev. E* **59**, 5457–5467.
- MARCUS, P. S. 1984a Simulation of Taylor-Couette flow. Part 1. numerical methods and comparison with experiment. *J. Fluid Mech.* **146**, 45–64.
- MARCUS, P. S. 1984b Simulation of Taylor-Couette flow. Part 2. numerical results for wavy-vortex flow with one travelling wave. *J. Fluid Mech.* **146**, 65–113.
- MOSER, R. D. & MOIN, P. 1987 The effects of curvature in wall-bounded turbulent flows. *J. Fluid Mech.* **175**, 479–510.
- MOULIC, S. G. & YAO, L. S. 1996 Taylor-Couette instability of travelling waves with a continuous spectrum. *J. Fluid Mech.* **324**, 181–198.
- MUJUMDAR, A. K. & SPALDING, D. B. 1977 Numerical computation of Taylor vortices. *J. Fluid Mech.* **81**, 295–304.
- PARKER, J. & MERATI, P. 1996 An investigation of turbulent Taylor-Couette flow using laser Doppler velocimetry in a refractive index matched facility. *Trans. ASME: J. Fluids Engng* **118**, 810–818.
- RACINA, A. & KIND, M. 2006 Specific power and local micromixing times in turbulent Taylor-Couette flow. *Exps. Fluids* **41**, 513–522.
- RASHIDI, M. & BANERJEE, S. 1990 The effect of boundary conditions and shear rate on streak formation and breakdown in turbulent channel flows. *Phys. Fluids A* **2**, 1827–1838.
- RIEHELMANN, D. & NANBU, K. 1997 Three-dimensional simulation of wavy Taylor vortex flow by direct simulation Monte Carlo method. *Phys. Fluids* **9**, 811–813.
- RIGOPOULOS, J., SHERIDAN, J. & THOMPSON, M. C. 2003 State selection in Taylor-Couette flow reached with an accelerated inner cylinder. *J. Fluid Mech.* **489**, 79–99.
- ROBINSON, S. K. 1991 Coherent motions in the turbulent boundary layer. *Annu. Rev. Fluid Mech.* **23**, 601.
- SARIC, W. S. 1994 Görtler vortices. *Annu. Rev. Fluid Mech.* **26**, 379–409.
- SHE, Z.-S., REN, K., LEWIS, G. S. & SWINNEY, H. L. 2001 Scalings and structures in turbulent Couette-Taylor flow. *Phys. Rev. E* **64**, 016308.
- SMITH, C. R. & METZLER, S. P. 1983 The characteristics of low-speed streaks in the near-wall region of a turbulent boundary layer. *J. Fluid Mech.* **129**, 27–54.
- SMITH, G. P. & TOWNSEND, A. A. 1982 Turbulent Couette flow between concentric cylinders at large Taylor numbers. *J. Fluid Mech.* **123**, 187–217.
- VON STAMM, J., GERDTS, U., BUZUG, T. & PFISTER, G. 1996 Symmetry breaking and period doubling on a torus in the VLF regime in Taylor-Couette flow. *Phys. Rev. E* **54**, 4938–4957.

- SWEARINGEN, J. D. & BLACKWELDER, R. F. 1987 The growth and breakdown of streamwise vortices in the presence of a wall. *J. Fluid Mech.* **182**, 255.
- TAKEDA, Y. 1999 Quasi-periodic state and transition to turbulence in a rotating Couette system. *J. Fluid Mech.* **389**, 81–99.
- TAM, W. Y. & SWINNEY, H. L. 1987 Mass transport in turbulent Couette-Taylor flow. *Phys. Rev. A* **36**, 1374–1381.
- TAYLOR, G.I. 1923 Stability of a viscous liquid contained between two rotating cylinders. *Phil. Trans. R. Soc. Lond. A* **223**, 289.
- TONG, P., GOLDBURG, W. I., HUANG, J. S. & WITTEN, T. A. 1990 Anisotropy in turbulent drag reduction. *Phys. Rev. Lett.* **65**, 2780–2783.
- TOWNSEND, A. A. 1984 Axisymmetric Couette flow at large Taylor numbers. *J. Fluid Mech.* **144**, 329–362.
- VASTANO, J. A. & MOSER, R. D. 1991 Short-time Lyapunov exponent analysis and the transition to chaos in Taylor-Couette flow. *J. Fluid Mech.* **233**, 83–118.
- WEI, T., KLINE, E. M., LEE, S. H. K. & WOODRUFF, S. 1992 Görtler vortex formation at the inner cylinder in Taylor-Couette flow. *J. Fluid Mech.* **245**, 47–68.
- WENDT, F. 1933 Turbulente strömungen zwischen zwei rotierenden konaxialen zylindern. *Ing.-Arch.* **4**, 577–595.
- WILD, P. M., DJILALI, N. & VICKERS, G. W. 1996 Experimental and computational assessment of windage losses in rotating machinery. *Trans. ASME: J. Fluids Engng* **118**, 116–122.